Journal of Applied Analysis and Computation
Volume 17, Number 1, February 2027, 119–144
Website:http://www.jaac-online.com
DOI:10.11948/20260074

RESEARCH ON ANALYTICAL SOLUTION, DYNAMIC ANALYSIS AND PORT ENGINEERING APPLICATION OF THE SIMPLIFIED MODIFIED CAMASSA-HOLM EQUATION (SMCH) UNDER FRACTIONAL DERIVATIVES

Hongwei Ma[1], Ziming Liu[1], Hongsheng Ma[2,3] and Jianming Qi[1,†]

Abstract To accurately characterize the nonlinear dynamic behavior of shallow water waves, this study focuses on the Simplified Modified Camassa-Holm (SMCH) equation with Conformable Fractional Derivative (CFD), and applies the extended tanh-function method to the analytical solution of this equation for the first time in our best knowledge. Through traveling wave transformation and homogeneous balance method, various analytical solutions are derived, including single-peak solitons, composite double-peak solitons, single-peak with shoulder solitons, and periodic soliton trains. Using MATLAB, 3D and 2D visualization models are constructed to systematically analyze the regulatory mechanisms of fractional order α and free parameter ω on wave field propagation characteristics, energy distribution, and morphological stability. To verify the effectiveness of the model, this study establishes a comparative system consisting of various fractional derivative forms, which confirms that the CFD has distinct advantages in local detail simulation and computational stability. Combining phase diagrams and Lyapunov exponents, the evolution law of the equation from periodic motion to chaotic state is revealed for the first time. Two numerical methods, fourth-order Runge-Kutta (RK44) and sixth-order accurate Huta86, are used to verify the reliability of the analytical solutions. The maximum absolute error of Huta86 is less than 2×10^{-12}, which is two orders of magnitude more accurate than RK44. The research results improve the solution system of fractional shallow water wave equations and provide accurate theoretical support and parameter optimization basis for wave load prediction and protective structure design in port and coastal engineering.

Keywords Simplified modified camassa-holm equation, fractional derivatives, extended tanh-function method, soliton solutions, dynamic analysis.

MSC(2010) 35R11, 35C07, 35Q53, 37N10, 76B15.

[†]The corresponding author.
[1]Business School, Shanghai DianJi University, 300 Shuihua Road, Pudong New Area, Shanghai 201306, China
[2]School of Transportation and Logistics, Southwest Jiaotong University, Chengdu 611756, China
[3]Shenzhen General Integrated Transportation and Municipal Engineering Design and Research Institute Co., Ltd, Shenzhen 518003, China
[*]The work presented in this paper was supported by the National Natural Science Foundation of China (11326083).
Email: mahw@sdju.edu.cn(H. Ma), lzm297312@163.com(Z. Liu), mahongs2025@163.com(H. Ma), qijianmingsdju@163.com(J. Qi)

1. Introduction and main results

Modeling the intricate dynamics of nonlinear wave phenomena in shallow waters remains a central challenge in fluid mechanics, captivating researchers for well over half a century [22, 38]. The mathematical representation of these complex motions, as with many physical systems, predominantly relies on the framework of partial differential equations [7, 17, 20, 21, 45, 57]. Numerous specific wave equations have been derived to capture distinct aspects of the phenomenon, including but not limited to the Green-Naghdi equations [26, 30], the Fornberg-Whitham equation [29, 52], the Serre-Green-Naghdi equations [8, 23, 31], the shallow water equations with varying topography [14, 37], the Degasperis–Procesi equation [24, 39], and the Ostrovsky Equation [44, 55]. Furthermore, Roberto Camassa and Darryl D. Holm introduced a completely integrable dispersive shallow-water equation in 1993 [11]:

$$U_t + 2kU_x - U_{xxt} + 3UU_x = 2U_xU_{xx} + UU_{xxx}. \tag{1.1}$$

In the Camassa-Holm (CH) equation, where $U = U(x,t)$ represents the fluid velocity field and the constant k is associated with the critical propagation speed of shallow water waves. This equation has become an important tool for simulating nearshore and harbor engineering due to its ability to effectively describe the interaction and breaking processes of solitary waves in shallow water hydrodynamics [25, 64]. Scholars have conducted extensive theoretical research on the CH equation, covering a wide range of core issues including the existence of global conservative solutions [18], extensions of the equation form [66], inverse scattering transform methods [65], construction of conservation laws [9], long-time asymptotic behavior of solutions [13], properties of peakon solutions [59], infinite propagation speed [40], and effects of noise [3]. Additionally, modifying and simplifying the original equation is also a key focus of research. The modified Camassa-Holm (MCH) equation proposed by Abdul-Majid Wazwaz in 2006 [62] is a representative example of such work, and its form is as follows:

$$U_t - U_{xxt} + 3U^2U_x - 2U_xU_{xx} - UU_{xxx} = 0. \tag{1.2}$$

Simplification of the preceding equation yields the SMCH [32]:

$$U_t + 2kU_x - U_{xxt} + \mu U^2U_x = 0, \tag{1.3}$$

where k and μ are non-zero constants.

Fractional calculus finds extensive utilization across scientific and engineering domains, particularly for modeling complex dynamic systems and nonlinear behaviors in physics, engineering, materials science, viscoelasticity, and electromagnetism [6, 28, 41, 56, 58]. Its broad applicability has made it increasingly prominent in research over the past few decades. Commonly used fractional derivative operators in the literature include the Riemann-Liouville [5, 63], Caputo [27], and Caputo-Fabrizio [34] derivatives. Recent studies in ocean engineering [19, 43, 60] have focused on solving for soliton solutions using CFD, M-truncated Fractional Derivative (MFD) and Modified Riemann-Liouville Derivative (MRLD) models. However, there remains a lack of research that combines and compares these novel derivative operators. This study aims to partially fill this gap. Therefore, analytically or numerically solving differential equations involving such derivatives is of significant importance.

Definition 1.1. Let $z : [0,\infty) \to \mathbb{R}$ be a function. Local CFD of $z(y)$ with α order is defined as follows [35]:

$$\mathcal{D}_y^{\alpha} z(y) = \lim_{h\to 0} \frac{z(y + hy^{1-\alpha}) - z(y)}{h}, \tag{1.4}$$

where $\alpha \in (0,1]$, $y > 0$.

Lemma 1.1. *Let $\phi(y)$ and $\psi(y)$ be $\alpha-$differentiable functions for $\alpha \in (0,1]$, $y > 0$. Then [62],*

(i) $\mathcal{D}_y^\alpha(m\phi(y) + n\psi(y)) = m\mathcal{D}_y^\alpha\phi(y) + n\mathcal{D}_y^\alpha\psi(y)$, $m, n \in \mathbb{R}$.

(ii) $\mathcal{D}_y^\alpha(y^n) = ny^{n-\alpha}$, $n \in \mathbb{R}$.

(iii) *If $\phi(y) = m$ in which m is a constant, then* $\mathcal{D}_y^\alpha(m) = 0$.

(iv) $\mathcal{D}_y^\alpha(\psi(y)\phi(y)) = \psi(y)\mathcal{D}_y^\alpha\phi(y) + \phi(y)\mathcal{D}_y^\alpha\psi(y)$.

(v) $\mathcal{D}_y^\alpha(\dfrac{\phi(y)}{\psi(y)}) = \dfrac{\psi(y)\mathcal{D}_y^\alpha\phi(y) - \phi(y)\mathcal{D}_y^\alpha\psi(y)}{\psi^2(y)}$, $\psi(y) \neq 0$.

(vi) *If the first derivative of $\phi(y)$ exists, then* $\mathcal{D}_y^\alpha(\phi(y)) = y^{1-\alpha}\dfrac{d\phi(y)}{dy}$.

Definition 1.2. In this section, we deal with the SMCH equation under CFD. Conformable fractional SMCH equation can be written as follows [1]:

$$\mathcal{D}_t^\alpha U + \lambda\mathcal{D}_x^\alpha U - \mathcal{D}_{xxt}^{3\alpha}U + \mu\mathcal{D}_t^\alpha U^3 = 0. \tag{1.5}$$

Where $U = U(x,t)$ denotes the wave function, with λ and μ representing non-zero real parameters.

Lemma 1.2. *The wave transformations employed are:*

$$U(x,t) = \theta(\delta),\ \ \delta = \frac{x^\alpha}{\alpha} - \omega\frac{t^\alpha}{\alpha}. \tag{1.6}$$

Here ω serves both as the wave speed parameter in the traveling wave transformation and as a non-zero undetermined constant.

Inserting the wave transformations in Eq. (1.6) to Eq. (1.5), we obtain the following nonlinear ODE:

$$\omega\theta''(\delta) + \mu\theta^3(\delta) + (\lambda - \omega)\theta(\delta) = 0. \tag{1.7}$$

This paper aims to derive analytical solutions for the SMCH equation with CFD. Within the scope of my knowledge, this is the first study to apply the extended tanh-function method [4] to the SMCH equation with CFD. This method has been effectively utilized in several nonlinear systems, such as the Korteweg-de Vries equation [47], coupled higher-order nonlinear Schrödinger equation [54], modified Korteweg-de Vries equation [61], Boussinesq-type equations [49], Klein-Gordon Equation [53], space-time fractional equal width wave equation [48], Kundu–Mukherjee–Naskar equation [10], and the perturbed Radhakrishnan-Kundu-Lakshmanan equation [46]. Existing studies on the SMCH equation have employed methods including the modified auxiliary equation method and the extended $\left(\frac{G'}{G^2}\right)$-expansion method [2], first integral method and exponential function method [33], the new $(m + 1/G')$-expansion method [36], the fractional reduced differential transform method [50].

2. Mathematical calculation

2.1. The extended tanh method

Consider the general form of the conformable PDE:

$$F\left(\mathcal{D}_x^\alpha U,\ \mathcal{D}_t^\alpha U,\ \mathcal{D}_x^\alpha\mathcal{D}_t^\alpha U, \ldots\right) = 0, \quad 0 < \alpha \leq 1. \tag{2.1}$$

For Eq. (2.1), F is a polynomial that contains the unknown function $U(x,t)$, $\mathcal{D}_*^{\alpha}U$ denote α order conformable of U about variables (x or t). This polynomial includes terms that exhibit nonlinear characteristics as well as higher-order derivatives. Subsequently, using the extended tanh method described in [4], we derive the exact solutions of the aforementioned SMCH equation.

Step 1. Inserting the traveling wave transformation; $T : U(x,t) = \theta(\delta)$, $\delta = \frac{x^{\alpha}}{\alpha} - \omega\frac{t^{\alpha}}{\alpha}$ into Eq. (2.1). Accordingly, Eq. (2.1) is transformed into the following relation:

$$K\big(\theta, \theta', \theta'', \dots\big) = 0. \tag{2.2}$$

In Eq. (9), K is a polynomial of $\theta(\delta)$ and its derivatives. where θ is the unknown functions of δ and the superscripts represent ordinary differential operator $\frac{d}{d\delta}$.

Step 2. The solution of Eq. (9) can be expressed as a polynomial of $\phi(\delta)$ according to [4],

$$\theta(\delta) = D_0 + \sum_{i=1}^{N}\left(D_i\phi^i(\delta) + E_i\phi^{-i}(\delta)\right). \tag{2.3}$$

It is learned from [4] that the polynomial of $\phi(\delta)$ satisfies the Riccati equation:

$$\frac{d\phi}{d\delta} = \varrho + \phi^2. \tag{2.4}$$

Step 3. After substituting Eq. (10) into Eq. (9) and making use of Eq. (11), Eq. (9) turns into a different polynomial format with respect to $\phi(\delta)$. By making the coefficients of each polynomial term equal to zero, a system of algebraic equations was obtained that involved the variables $D_0 \dots D_n$, $E_1 \dots E_n$.

Step 4. The specific values of the unknowns $D_0, \dots, D_n$ and $E_1, \dots, E_n$ can be determined from the system of algebraic equations obtained in Step 3. [4] provides five explicit solutions for $\phi(\delta)$.

Lemma 2.1. *The Riccati equation solutions are:*

- ***Case 1*** *($\varrho < 0$):*

$$\begin{aligned}\phi(\delta) &= -\sqrt{-\varrho}\,\tanh(\sqrt{-\varrho}\delta),\\ \phi(\delta) &= -\sqrt{-\varrho}\,\coth(\sqrt{-\varrho}\delta).\end{aligned} \tag{2.5}$$

- ***Case 2*** *($\varrho = 0$):*

$$\phi(\delta) = -\frac{1}{\delta}. \tag{2.6}$$

- ***Case 3*** *($\varrho > 0$):*

$$\begin{aligned}\phi(\delta) &= \sqrt{\varrho}\tan(\sqrt{\varrho}\delta),\\ \phi(\delta) &= -\sqrt{\varrho}\cot(\sqrt{\varrho}\delta).\end{aligned} \tag{2.7}$$

Step 5. By applying the inverse transformation T^{-1}, we can obtain the solution $\theta(\delta)$, where $\delta = \frac{x^{\alpha}}{\alpha} - \omega\frac{t^{\alpha}}{\alpha}$. In this manner, the exact solutions of the SMCH equation can be derived. By setting $U(x,t) = \theta(\delta)$, we obtain the analytical solutions of the SMCH nonlinear wave equation.

2.2. Employing the extended tanh method to the Eq. (1.7)

Theorem 2.1. *The exponent $m = 1$ emerges as a consequence of homogeneous equilibrium balancing between the θ^3 and θ'' components in Eq. (2.1). We put forth candidate solutions for Eq. (1.7) in the following form:*

$$\theta(\delta) = D_0 + D_1\phi(\delta) + \frac{E_1}{\phi(\delta)}, \tag{2.8}$$

here the unknown constants D_0, D_1, E_1 are to be determined subsequently.

Terms sharing the same exponent of $\theta(\delta)$ are methodically grouped and then integrated utilizing the expressions provided in Eq. (2.8) and Eq. (2.4).

Employing Eq. (2.8), we derive

$$\theta'(\xi) = \phi'(\xi)(D_1 - E_1\phi^{-2}(\xi)), \tag{2.9}$$

$$\theta''(\xi) = \phi''(\xi)(D_1 - E_1\phi^{-2}(\xi)) + 2E_1(\phi'(\xi))^2\phi^{-3}(\xi). \tag{2.10}$$

Here, Eq. (2.10) and Eq. (2.8) supersede Eq. (1.7), with systematic integration of all terms featuring identical exponents of $\theta(\delta)$.

$$\begin{aligned}&\left(\mu D_1^3 + 2\omega D_1\right)\phi(\delta)^3 + 3\mu D_0 D_1^2\phi(\delta)^2 + \left(3\mu D_0^2 D_1 + 3\mu D_1^2 E_1 + 2\omega D_1\rho + \lambda D_1 - \omega D_1\right)\phi(\delta)\\&+ \mu D_0^3 + 6\mu D_0 D_1 E_1 + \lambda D_0 - \omega D_0 + \frac{3\mu D_0^2 E_1 + 3\mu D_1 E_1^2 + 2\omega E_1\rho + \lambda E_1 - \omega E_1}{\phi(\delta)}\\&+ \frac{3\mu D_0 E_1^2}{\phi(\delta)^2} + \frac{\mu E_1^3 + 2\omega E_1\rho^2}{\phi(\delta)^3} = 0.\end{aligned} \tag{2.11}$$

Subsequently, indeterminate coefficients associated with identical terms in the $\theta(\delta)$ expansions are methodically eliminated, whereupon the resulting equation system is solved:

$$\begin{cases}\mu D_1^3 + 2\omega D_1 = 0,\\ 3\mu D_0 D_1^2 = 0,\\ 3\mu D_0^2 D_1 + 3\mu D_1^2 E_1 + 2\omega D_1\rho + \lambda D_1 - \omega D_1 = 0,\\ \mu D_0^3 + 6\mu D_0 D_1 E_1 + \lambda D_0 - \omega D_0 = 0,\\ 3\mu D_0^2 E_1 + 3\mu D_1 E_1^2 + 2\omega E_1\rho + \lambda E_1 - \omega E_1 = 0,\\ 3\mu D_0 E_1^2 = 0,\\ \mu E_1^3 + 2\omega E_1\rho^2 = 0.\end{cases} \tag{2.12}$$

Case 1. We obtain $D_0{=}0, D_1{=}0, E_1{=}E_1, \lambda{=} - 2\omega\rho + \omega, \mu{=} - \frac{2\omega\,\rho^2}{E_1^2}, \omega{=}\omega, \rho{=}\rho$, inserting all above coefficients into Eq. (2.8) yields, four distinct soliton solution profiles emerge:

$$\begin{aligned}U_{1.1}(x,t) = \theta_{1.1}(\delta) = E_1(\sqrt{-\rho}\tanh\left(\sqrt{-\rho}\delta\right))^{-1}, \rho < 0,\\ U_{1.2}(x,t) = \theta_{1.2}(\delta) = E_1(\sqrt{-\rho}\coth\left(\sqrt{-\rho}\delta\right))^{-1}, \rho < 0,\\ U_{1.3}(x,t) = \theta_{1.3}(\delta) = E_1(\sqrt{\rho}\tan\left(\sqrt{\rho}\delta\right))^{-1}, \rho > 0,\\ U_{1.4}(x,t) = \theta_{1.4}(\delta) = E_1(-\sqrt{\rho}\cot\left(\sqrt{\rho}\delta\right))^{-1}, \rho > 0.\end{aligned} \tag{2.13}$$

Case 2. We get $D_0{=}0, D_1{=}D_1, E_1{=}0, \lambda{=}-\omega\,(2\rho-1)\,, \mu{=}-\frac{2\omega}{D_1^2}, \omega{=}\omega, \rho{=}\rho$, inserting all above coefficients into Eq. (2.8) yields, four distinct soliton solution profiles emerge:

$$\begin{aligned}
U_{2.1}(x,t) &= \theta_{2.1}(\delta) = D_1(\sqrt{-\rho}\tanh\left(\sqrt{-\rho}\delta\right)), \rho<0,\\
U_{2.2}(x,t) &= \theta_{2.2}(\delta) = D_1(\sqrt{-\rho}\coth\left(\sqrt{-\rho}\delta\right)), \rho<0,\\
U_{2.3}(x,t) &= \theta_{2.3}(\delta) = D_1(\sqrt{\rho}\tan\left(\sqrt{\rho}\delta\right)), \rho>0,\\
U_{2.4}(x,t) &= \theta_{2.4}(\delta) = D_1(-\sqrt{\rho}\cot\left(\sqrt{\rho}\delta\right)), \rho>0.
\end{aligned} \tag{2.14}$$

Case 3. We also get $D_0{=}0, D_1{=}D_1, E_1{=}D_1\rho, \lambda{=}\omega\,(4\rho+1)\,, \mu{=}-\frac{2\omega}{D_1^2}, \omega{=}\omega, \rho{=}\rho$, inserting all above coefficients into Eq. (2.8) yields, four distinct soliton solution profiles emerge:

$$\begin{aligned}
U_{3.1}(x,t) &= \theta_{3.1}(\delta) = D_1(\sqrt{-\rho}\tanh\left(\sqrt{-\rho}\delta\right)) + D_1\rho(\sqrt{-\rho}\tanh\left(\sqrt{-\rho}\delta\right))^{-1}, \rho<0,\\
U_{3.2}(x,t) &= \theta_{3.2}(\delta) = D_1(\sqrt{-\rho}\coth\left(\sqrt{-\rho}\delta\right)) + D_1\rho(\sqrt{-\rho}\coth\left(\sqrt{-\rho}\delta\right))^{-1}, \rho<0,\\
U_{3.3}(x,t) &= \theta_{3.3}(\delta) = D_1(\sqrt{\rho}\tan\left(\sqrt{\rho}\delta\right)) + D_1\rho(\sqrt{\rho}\tan\left(\sqrt{\rho}\delta\right))^{-1}, \rho>0,\\
U_{3.4}(x,t) &= \theta_{3.4}(\delta) = D_1(-\sqrt{\rho}\cot\left(\sqrt{\rho}\delta\right)) + D_1\rho(-\sqrt{\rho}\cot\left(\sqrt{\rho}\delta\right))^{-1}, \rho>0.
\end{aligned} \tag{2.15}$$

Case 4. We also get $D_0{=}0, D_1{=}D_1, E_1{=}-D_1\rho, \lambda{=}-\omega\,(8\rho-1)\,, \mu{=}-\frac{2\omega}{D_1^2}, \omega{=}\omega, \rho{=}\rho$, inserting all above coefficients into Eq. (2.8) yields, four distinct soliton solution profiles emerge:

$$\begin{aligned}
U_{4.1}(x,t) &= \theta_{4.1}(\delta) = D_1(\sqrt{-\rho}\tanh\left(\sqrt{-\rho}\delta\right)) - D_1\rho(\sqrt{-\rho}\tanh\left(\sqrt{-\rho}\delta\right))^{-1}, \rho<0,\\
U_{4.2}(x,t) &= \theta_{4.2}(\delta) = D_1(\sqrt{-\rho}\coth\left(\sqrt{-\rho}\delta\right)) - D_1\rho(\sqrt{-\rho}\coth\left(\sqrt{-\rho}\delta\right))^{-1}, \rho<0,\\
U_{4.3}(x,t) &= \theta_{4.3}(\delta) = D_1(\sqrt{\rho}\tan\left(\sqrt{\rho}\delta\right)) - D_1\rho(\sqrt{\rho}\tan\left(\sqrt{\rho}\delta\right))^{-1}, \rho>0,\\
U_{4.4}(x,t) &= \theta_{4.4}(\delta) = D_1(-\sqrt{\rho}\cot\left(\sqrt{\rho}\delta\right)) - D_1\rho(-\sqrt{\rho}\cot\left(\sqrt{\rho}\delta\right))^{-1}, \rho>0.
\end{aligned} \tag{2.16}$$

3. Computational frameworks for comparative study of physical phenomena

Singular solutions typically carry enhanced physical significance. Consequently, based on multi-dimensional visualization from computational simulations, selected exact solutions are analyzed via Matlab R2024a to elucidate their physical implications and structural properties:

3.1. Computational modeling analysis of fractional component impacts

To quantify the influence of the fractional derivative order α on the dynamic characteristics of shallow water waves, this study systematically analyzes the physical properties and structural evolution laws of analytical solutions to the SMCH equation (corresponding to the shallow water wave velocity field $U(x,t)$) under different α values based on the numerical simulation and visualization results of Figures 1-5. The core conclusions and engineering significance are as follows:

Figures 1-2 reveal the regulation of α on the propagation and stability of the solitary wave velocity field: At low α(0.25-0.45), the waveform is gentle with a small velocity gradient and obvious energy diffusion, corresponding to the nearshore weak nonlinear wave scenario where the water flow velocity changes gently but the stability is poor; at high α(0.75-0.85), the waveform edges are steep with concentrated energy and slow amplitude decay, which is consistent with

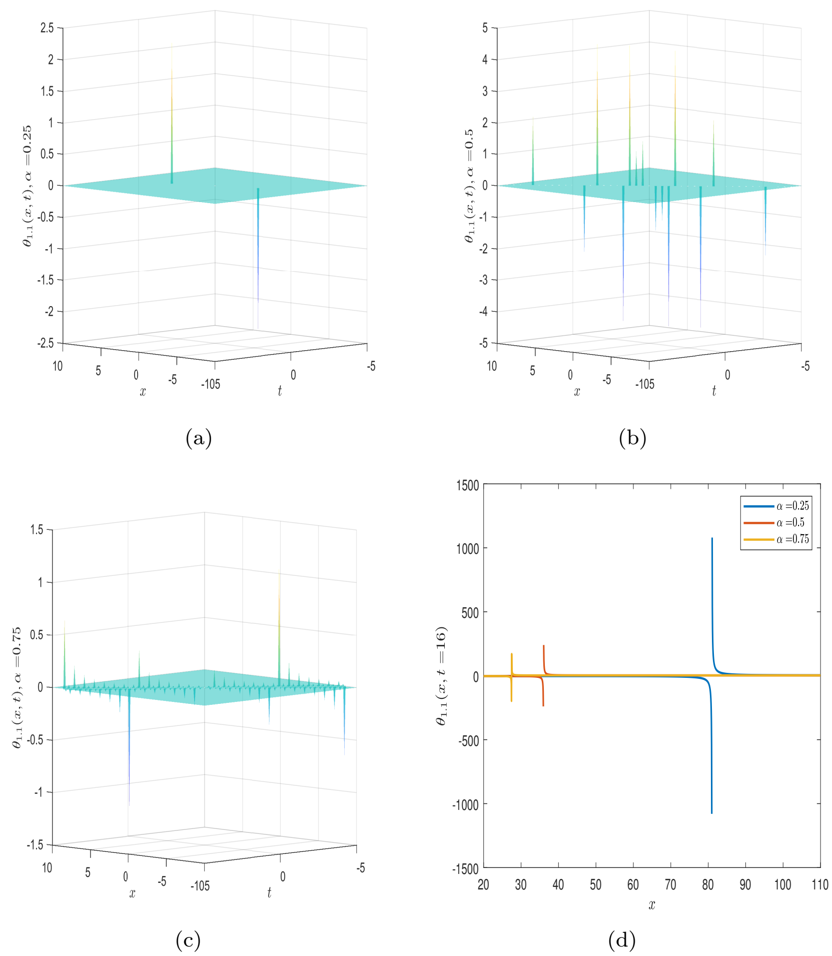

Figure 1. Figure (a)-(c) are three-dimensional diagrams by $\theta_{1.1}(x,t;\alpha)$. Figure (d) is the two-dimensional diagram when $t = 16$. The $E_1 = 2, \rho = -1, \omega = 1.5$ and (a): $\alpha = 0.25$; (b): $\alpha = 0.50$; (c): $\alpha = 0.75$.

the actual scenario of strong solitary waves impacting the shoreline in port engineering and can improve the accuracy of wave load prediction. Figure 3 illustrates the optimization of α on the regularity of the periodic wave field: At low α, the periodic wave has a low frequency and uneven wave crest heights, corresponding to the irregular wave groups disturbed by wind in the open sea; at high α, the periodic wave frequency increases and the wave crests are uniform, matching the regular wave groups constrained by breakwaters, which provides theoretical support for the calculation of periodic impact loads on wharves. Figures 4-5 analyze the influence of α on multi-wave interaction and solitary wave breaking: At low α, the composite double-peak wave has unbalanced energy and weak interaction, while the single-peak with shoulder wave has significant secondary disturbance and is prone to breaking; at high α, the double peaks have balanced energy and enhanced interaction, and the secondary disturbance of the single-peak with shoulder wave is suppressed with improved anti-breaking capability. The breaking risk of solitary waves under different water depths can be predicted by adjusting α.

In summary, the order effect of α dominates the energy aggregation and diffusion charac-

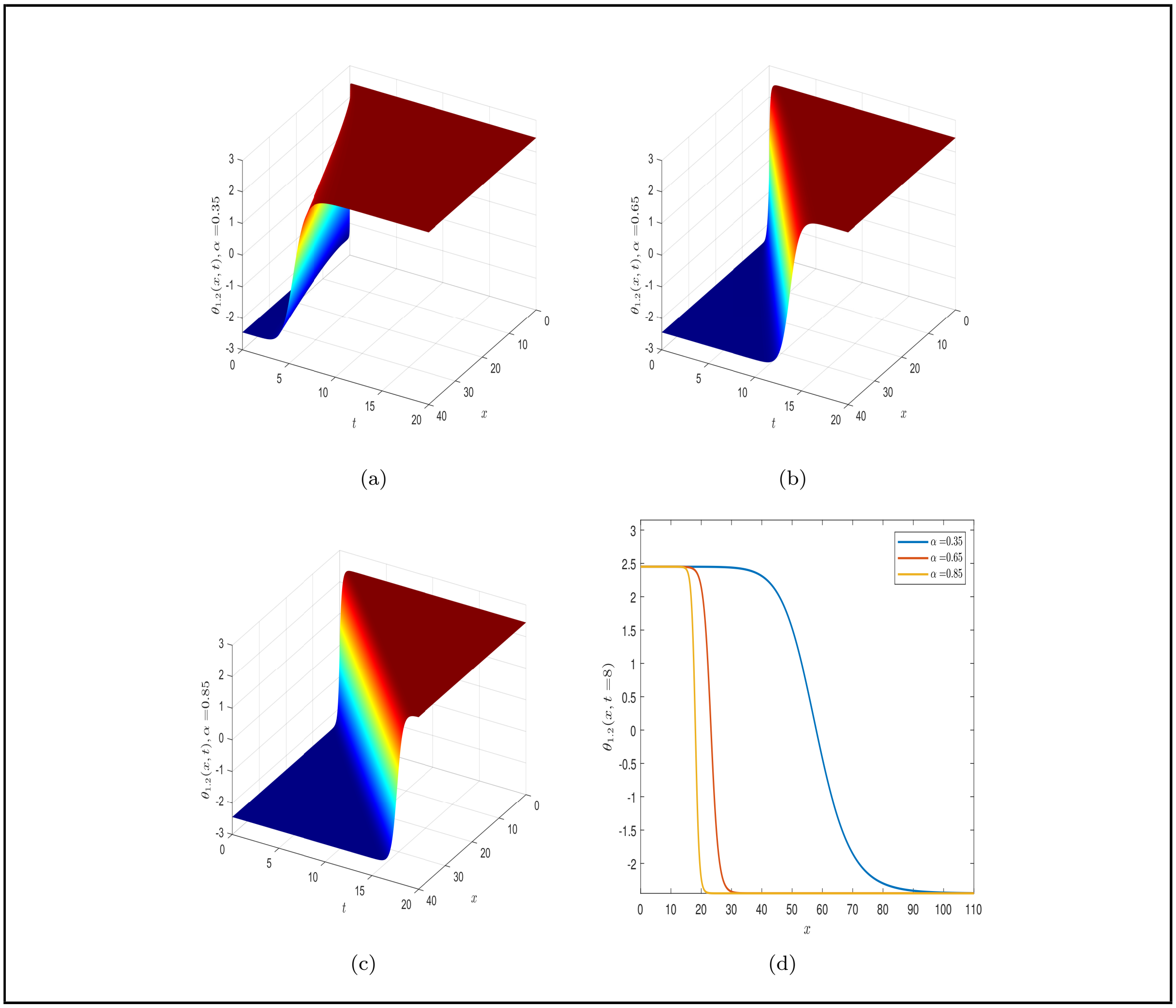

Figure 2. Figure (a)-(c) are three-dimensional diagrams by $\theta_{1.2}(x,t;\alpha)$. Figure (d) is the two-dimensional diagram when $t = 8$. The $E_1 = 3, \rho = -1.5, \omega = 2$ and (a): $\alpha = 0.35$; (b): $\alpha = 0.65$; (c): $\alpha = 0.85$.

teristics of the wave field by regulating the sensitivity of the conformable fractional derivative to the rate of change of the velocity field. The visualization results of Figures 1-5 provide key support for engineering practice: The α parameter can be adjusted to match different scenarios such as nearshore weak nonlinear waves and port strong solitary waves, providing an accurate velocity field reference for port and coastal engineering such as breakwater design and wave load prediction.

3.2. Influences of free parameters

The core physical significance of Figure 6 lies in revealing the regulatory effect of the free parameter ω (possessing the dual attributes of being both a wave speed parameter in the traveling wave transformation and a non-zero undetermined constant in the equation) on the soliton profiles of the SMCH equation with CFD, clarifying its quantitative correlation with the propagation characteristics and amplitude magnitude of shallow water waves, and providing a parameter

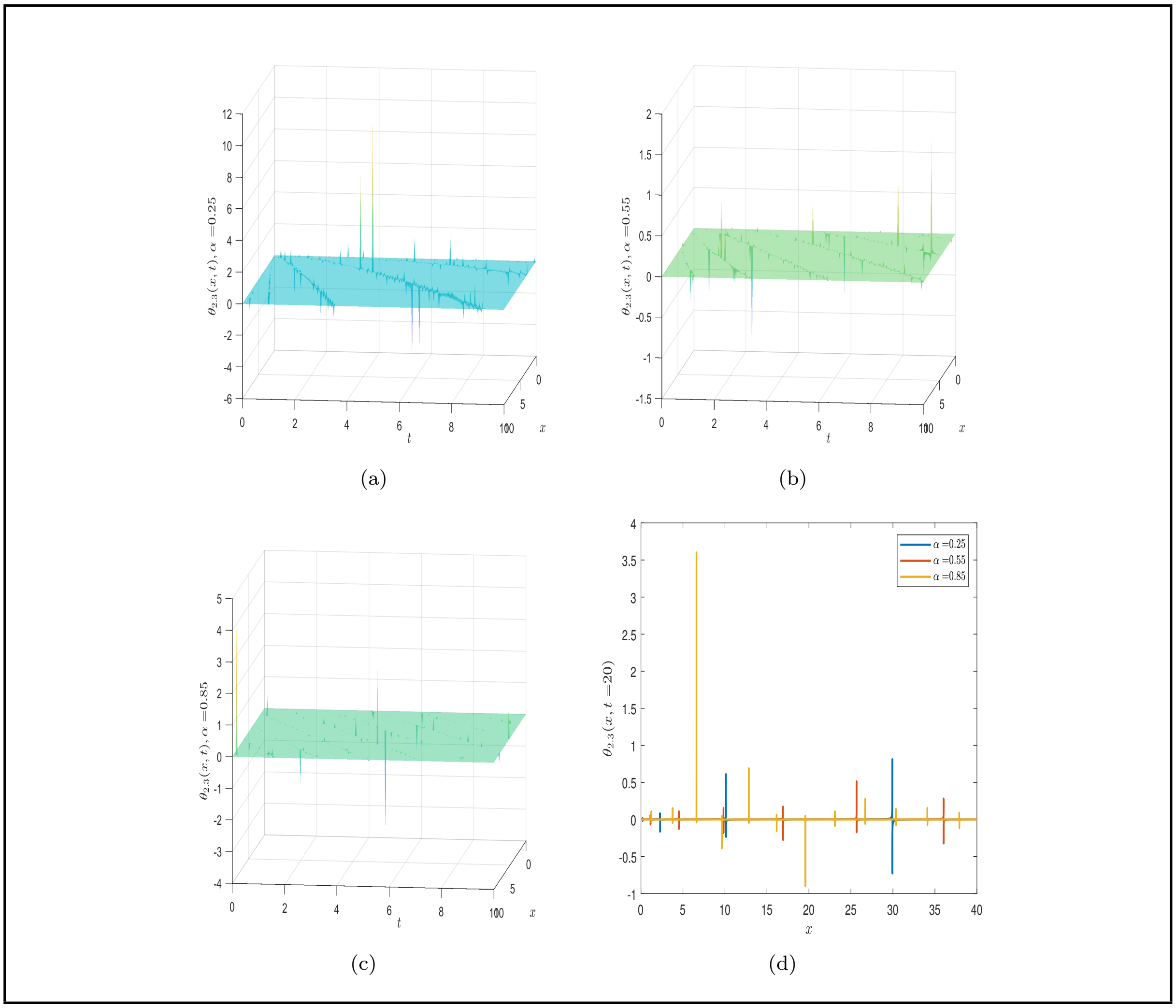

Figure 3. Figure (a)-(c) are three-dimensional diagrams by $\theta_{2.3}(x,t;\alpha)$. Figure (d) is the two-dimensional diagram when $t = 20$. The $D_1 = 2, \rho = 2, \omega = 1.5$ and (a): $\alpha = 0.25$; (b): $\alpha = 0.55$; (c): $\alpha = 0.85$.

optimization basis for the engineering simulation of shallow water wave dynamics. Taking the soliton solutions $\theta_{1.1}(x,t;\alpha)$ and $\theta_{1.2}(x,t;\alpha)$ (both describing the shallow water wave velocity field $U(x,t)$ via the SMCH equation) as the research objects, this study fixes the fractional order α (0.50, 0.65) and parameters such as E_1 and ρ, while only varying the values of ω (Figure (a): 1, 1.5, 2; Figure (b): 1.5, 2.5, 3.5). By observing the influence of ω on the wave form through the absolute value distribution of the solutions, three key laws are derived: ω can regulate the wave propagation direction, and its increase drives the soliton to propagate along the positive x-axis, providing support for simulating the propagation path of waves in nearshore/port engineering; ω is positively correlated with the amplitude (e.g., the amplitude at $\omega = 3.5$ is significantly larger than that at $\omega = 1.5$), and since the amplitude corresponds to the energy intensity of the wave, adjusting ω can simulate waves of different intensities, offering references for the impact resistance design of structures such as breakwaters; waves maintain the basic soliton structure under different ω values, confirming that ω is an effective variable for regulating wave dynamics. In summary, Figure 6 clarifies the dual regulatory role of ω in “propagation direction + energy

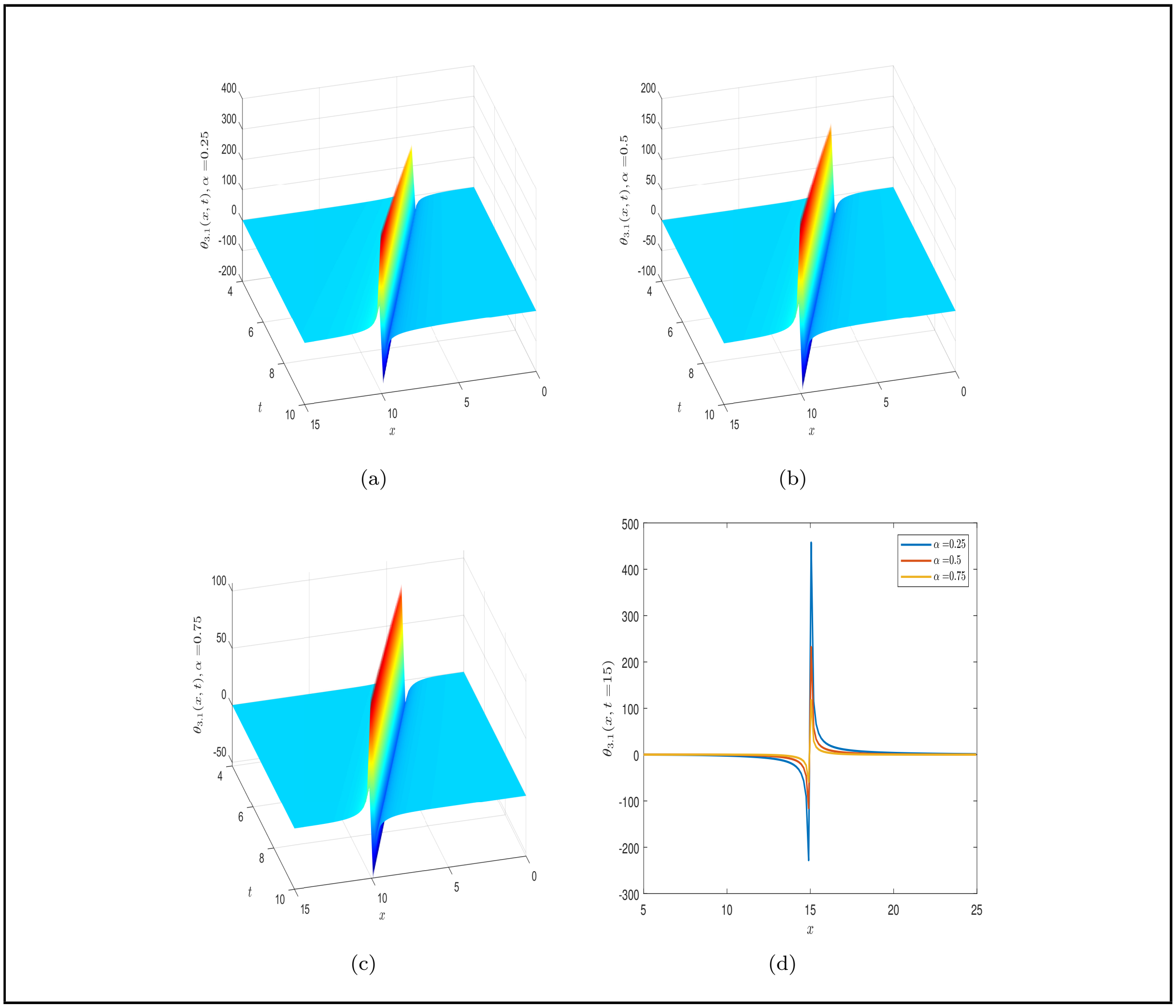

Figure 4. Figure (a)-(c) are three-dimensional diagrams by $\theta_{3.1}(x, t; \alpha)$. Figure (d) is the two-dimensional diagram when $t = 15$. The $D_1 = 3, \omega = 1, \rho = -1.5, E_1 = -4.5$ and (a): $\alpha = 0.25$; (b): $\alpha = 0.50$; (c): $\alpha = 0.75$.

intensity", improves the physical connotation of the equation's parameters, and provides a basis for the accurate simulation of shallow water waves and the optimization of engineering designs.

3.3. Comparative investigate with different fractional derivatives

Given the diverse definitions of fractional derivatives-including the CFD, MRLD, and MFD formulations-solutions to fractional models yield distinct physical interpretations and applications contingent upon associated fractional orders. The selection of optimal fractional operators presents significant challenges for researchers. Consequently, this study benchmarks solutions against MRLD and MFD formulations under respective transformations:

$$\text{MRLD:} \quad \theta(\delta), \quad \delta = \frac{x^\alpha}{\Gamma(1+\alpha)} - \omega\frac{t^\alpha}{\Gamma(1+\alpha)}, \tag{3.1}$$

$$\text{MFD:} \quad \theta(\delta), \quad \delta = \frac{\Gamma(1+\beta)}{\alpha}(x^\alpha - \omega t^\alpha). \tag{3.2}$$

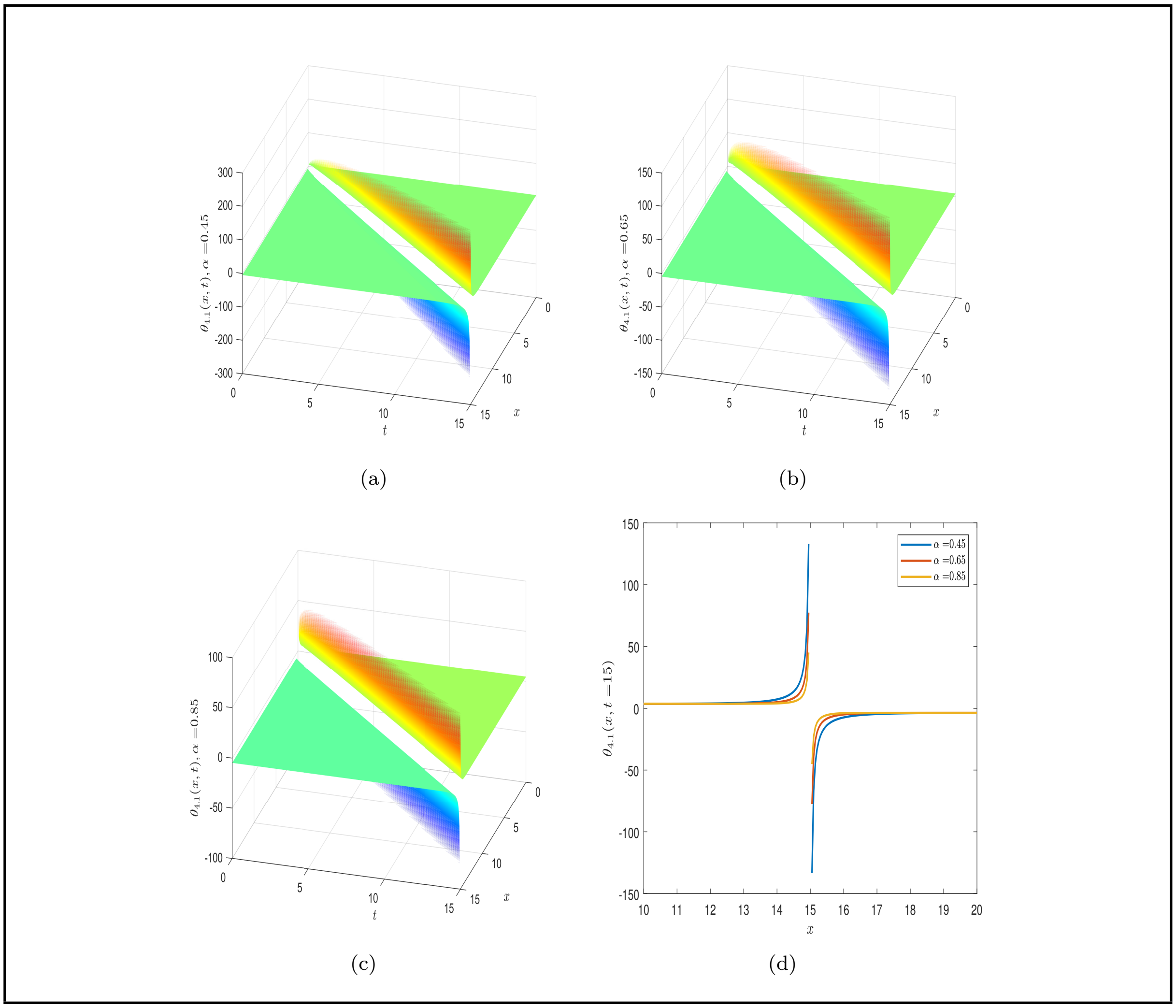

Figure 5. Figure (a)-(c) are three-dimensional diagrams by $\theta_{4.1}(x,t;\alpha)$. Figure (d) is the two-dimensional diagram when $t=15$. The $D_1=1.5, \omega=1, \rho=-2.5, E_1=3.75$ and (a): $\alpha=0.45$; (b): $\alpha=0.65$; (c): $\alpha=0.85$.

The fractional-order derivative via the MRLD approach adopts the following representation:

$$\theta_{1.2MRLD}(x,t) = E_1(\sqrt{-\rho}\coth(\sqrt{-\rho}(\frac{x^\alpha}{\Gamma(1+\alpha)} - \omega\frac{t^\alpha}{\Gamma(1+\alpha)}))^{-1}, \tag{3.3}$$

$$\begin{aligned}\theta_{4.1MRLD}(x,t) =& D_1(\sqrt{-\rho}\tanh(\sqrt{-\rho}(\frac{x^\alpha}{\Gamma(1+\alpha)} - \omega\frac{t^\alpha}{\Gamma(1+\alpha)})\\ &- D_1\rho(\sqrt{-\rho}\tanh(\sqrt{-\rho}(\frac{x^\alpha}{\Gamma(1+\alpha)} - \omega\frac{t^\alpha}{\Gamma(1+\alpha)}))^{-1}.\end{aligned} \tag{3.4}$$

The fractional-order derivative via the MFD approach adopts the following representation:

$$\theta_{1.2MFD}(x,t) = E_1(\sqrt{-\rho}\coth(\sqrt{-\rho}\frac{\Gamma(1+\beta)}{\alpha}(x^\alpha - \omega t^\alpha)))^{-1}, \tag{3.5}$$

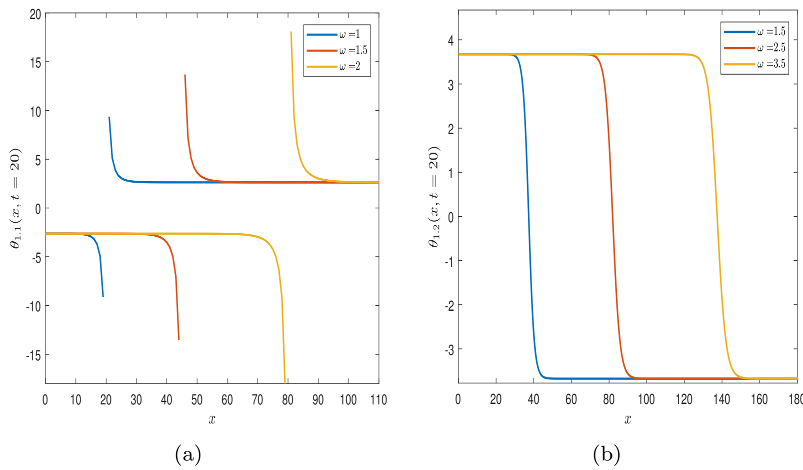

Figure 6. The effect of the free parameter ω on the solution profiles. Figure (a) The absolute value of the solution $\theta_{1.1}(x,t;\alpha)$ with $\alpha = 0.50$, $E_1 = 2$, $\rho = -1$. Figure (b) The absolute value of the solution $\theta_{1.2}(x,t;\alpha)$ with $\alpha = 0.65$, $D_1 = 3$, $\rho = -1.5$, $E_1 = -4.5$.

$$\begin{aligned}\theta_{4.1MFD}(x,t) =& D_1(\sqrt{-\rho}\tanh(\sqrt{-\rho}\frac{\Gamma(1+\beta)}{\alpha}(x^\alpha - \omega t^\alpha))) \\ & - D_1\rho(\sqrt{-\rho}\tanh(\sqrt{-\rho}\frac{\Gamma(1+\beta)}{\alpha}(x^\alpha - \omega t^\alpha)))^{-1}.\end{aligned} \tag{3.6}$$

By comparing these solutions with those from the MFD and MRLD models, it clarifies the differences in the influence of various fractional derivatives on the simulation of shallow water wave velocity fields, providing a basis for selecting appropriate models in engineering to ensure that the simulation of wave dynamic behaviors (such as propagation characteristics, amplitude stability, and morphological structure) is more consistent with practical scenarios.

From the perspective of Figure 7, this figure takes two typical solutions of the SMCH equation, i.e., $\theta_{1.2}(x,t)$ (twisted soliton solution) and $\theta_{4.1}(x,t)$ (single-peak with shoulder structure solution), as research objects, and presents the simulation differences among the three derivative models through 3D distribution diagrams and 2D cross-sectional diagrams. On one hand, the solutions of the CFD model are consistent with those of the MFD and MRLD models in terms of overall morphology and propagation trend, which confirms the physical rationality of the solutions to the SMCH equation with CFD and proves that this model can be used for shallow water wave simulation. On the other hand, the 2D cross-sectional diagrams show that the solutions of the CFD model are more consistent with practical engineering scenarios in terms of amplitude peaks, stability, and local details (e.g., the ratio between the shoulder structure and the main peak of $\theta_{4.1}$), while the MFD and MRLD models have slight deviations due to their inherent definition characteristics. This provides a basis for engineering applications: CFD is preferred for high-precision local velocity field simulation (such as the shoulder disturbance of strong solitary waves before impacting shorewalls); all three models can be used if the focus is on the overall propagation trend, but the CFD model has more prominent computational stability (without obvious energy dispersion or structural distortion). Meanwhile, the core dynamic characteristics (such as amplitude decay rate, propagation speed, and structural integrity) of the solutions from the three models are highly consistent, and the data fluctuation of the CFD model is smoother,

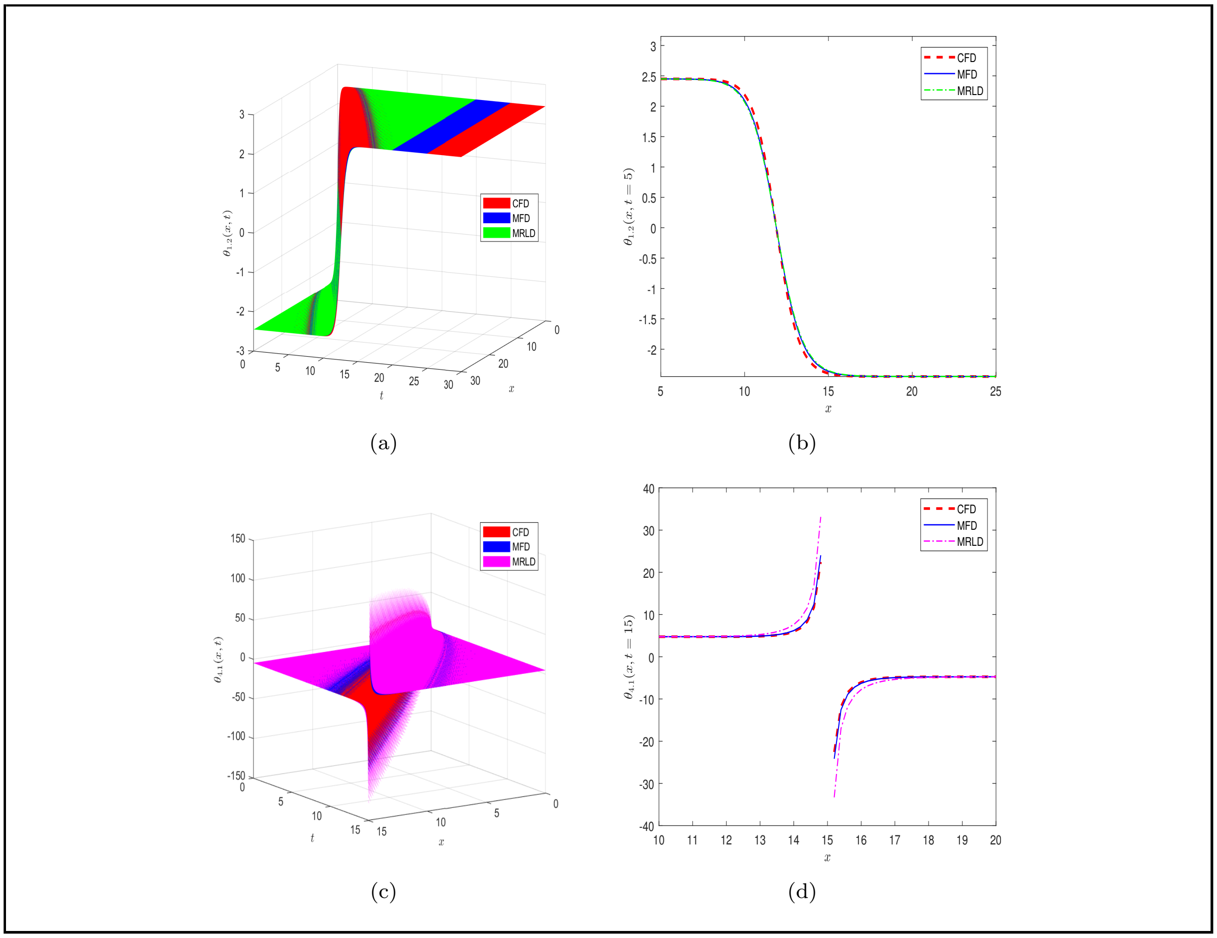

Figure 7. Comparison of the derived solutions $\theta_{1.2}(x,t)$ and $\theta_{4.1}(x,t)$ with MFD and MRLD of different fractional orders. Figure (a) Three-dimensional graphical representation of $\theta_{1.2}(x,t)$. Figure (b) Two-dimensional cross-sectional comparison of $\theta_{1.2}(x,t)$, with parameters: $\alpha = 0.8$, $\beta = 0.5$, $y = 0$, $E_1 = 3$, $\rho = -1.5$, $\omega = 2$, $c = -2$, $k = 1$, $t = 5$. Figure (c) Three-dimensional graphical representation of $\theta_{4.1}(x,t)$. Figure (d) Two-dimensional cross-sectional comparison of $\theta_{4.1}(x,t)$, with parameters: $\alpha = 0.6$, $\beta = 0.8$, $y = 0$, $D_1 = 1.5$, $\omega = 1$, $\rho = -2.5$, $E_1 = 3.75$, $c = -1$, $k = 1$, $t = 15$.

which further verifies the reliability of the SMCH equation with CFD and provides more accurate velocity field references for the design of port and coastal engineering-related projects.

In summary, Section 3.3 provides physical validity support for the SMCH equation with CFD through comparison. The visual results in Figure 7 prove that this model not only conforms to the general laws of fractional dynamics but also is more consistent with practical engineering in terms of local detail simulation, providing a direct basis for subsequent engineering model selection.

3.4. Phase diagram, Lyapunov exponent and chaos analysis

In this section, we begin by reformulating the question posed in Eq. (1.7) as the following differential system,

$$\begin{cases} \theta' = \eta, \\ \eta' = -\dfrac{\mu}{\omega}\theta^3 - \dfrac{\lambda - \omega}{\omega}\theta. \end{cases} \tag{3.7}$$

Eq. (3.7) reveals that if $\frac{\omega-\lambda}{\mu} > 0$ then the system has three equilibrium points, as follows: $A_0 = (0,0)$, $A_1 = (\sqrt{\frac{\omega-\lambda}{\mu}}, 0)$, $A_2 = (-\sqrt{\frac{\omega-\lambda}{\mu}}, 0)$. On the other hand, if $\frac{\omega-\lambda}{\mu} < 0$, the system has only one equilibrium point $A_0 = (0,0)$, in the real domain. From the expression of the above system, we can directly compute the corresponding Jacobian matrix, for convenience in the subsequent discussion, we denote it as $J(\theta,\eta)$, and the explicit result is as follows:

$$J(\theta,\eta) = \begin{pmatrix} 0 & 1 \\ -\dfrac{3\mu\theta^2+\lambda-\omega}{\omega} & 0 \end{pmatrix}. \tag{3.8}$$

The characteristic polynomial of the Jacobian matrix of the system can be obtained by evaluating $|J - \zeta I_2| = 0$. We present a detailed discussion of the eigenvalues corresponding to each distinct equilibrium point.

Case 1. When the equilibrium point is $A_0 = (0,0)$, the eigenvalues can be found by computing the characteristic polynomial $\zeta^2 + \frac{\lambda-\omega}{\omega} = 0$, where ζ denotes the eigenvalue. When $\frac{\omega-\lambda}{\omega} < 0$, the system has a pair of conjugate imaginary roots, namely $\zeta_{1,2} = \pm\sqrt{\frac{\lambda-\omega}{\omega}}i$; when $\frac{\omega-\lambda}{\omega} > 0$, the system has a pair of real roots, namely $\zeta_{1,2} = \pm\sqrt{\frac{\omega-\lambda}{\omega}}$. When the system possesses a pair of conjugate imaginary eigenvalues, the equilibrium is a center and the system is critically stable; once any eigenvalue acquires a positive real part, the equilibrium becomes a saddle and the system turns unstable. Therefore, when $\frac{\omega-\lambda}{\omega} > 0$, the equilibrium point $A_0 = (0,0)$ is a center; when $\frac{\omega-\lambda}{\omega} < 0$, it is a saddle.

Case 2. When the equilibrium point is $A_1 = (\sqrt{\frac{\omega-\lambda}{\mu}}, 0)$ or $A_2 = (-\sqrt{\frac{\omega-\lambda}{\mu}}, 0)$, the characteristic equation is $\zeta^2 + 2\frac{\omega-\lambda}{\omega} = 0$. When $\frac{\omega-\lambda}{\omega} > 0$, the system has a pair of conjugate imaginary roots, namely $\zeta_{1,2} = \pm\sqrt{\frac{2(\omega-\lambda)}{\omega}}i$; when $\frac{\omega-\lambda}{\omega} < 0$, the system has a pair of real roots, namely $\zeta_{1,2} = \pm\sqrt{\frac{2(\lambda-\omega)}{\omega}}$. Therefore, when $\frac{\omega-\lambda}{\omega} > 0$, the equilibrium point $A_1 = (\sqrt{\frac{\omega-\lambda}{\mu}}, 0)$ or $A_2 = (-\sqrt{\frac{\omega-\lambda}{\mu}}, 0)$ is a center; when $\frac{\omega-\lambda}{\omega} < 0$, it is a saddle.

Based on our previous analysis of the corresponding equilibrium points, regardless of whether it is A_0, A_1, or A_2, each has the potential to become either a center point or a saddle point when different parameters are selected. Figure 8(a) displays the phase diagram corresponding to eight different initial values when the parameters $\lambda = 1$, $\mu = 1$ and $\omega = 2$. It can be observed that in the phase space, the trajectories of the system exhibit periodic characteristics. This is because the selected parameters result in the system's eigenvalues being a pair of conjugate imaginary roots. Consequently, the system neither expands nor contracts indefinitely but instead demonstrates periodic behavior, as specifically shown in Figure 8(a) and Figure 8(b). For Figure 8(c), it can be observed that the equilibrium point A_0 in the phase space is a saddle point. This is because the selected parameters $\lambda = 1$, $\mu = 1$ and $\omega = 2$ satisfy the condition $\frac{\omega-\lambda}{\omega} > 0$, resulting in the system having a pair of positive and negative real eigenvalues i.e. $\zeta_{1,2} = \pm\sqrt{\frac{1}{2}}$. Consequently, the system is unstable and the corresponding equilibrium point is a saddle point. Figure 8(c)-(d) effectively validate the theoretical analysis.

When different initial conditions are taken near the equilibrium point A_1, and the parameters are set to $\lambda = 1$, $\mu = 1$ and $\omega = 2$, the eigenvalues of the system form a pair of conjugate imaginary roots i.e. $\zeta = \pm i$. As a result, the system exhibits periodic behavior, as specifically

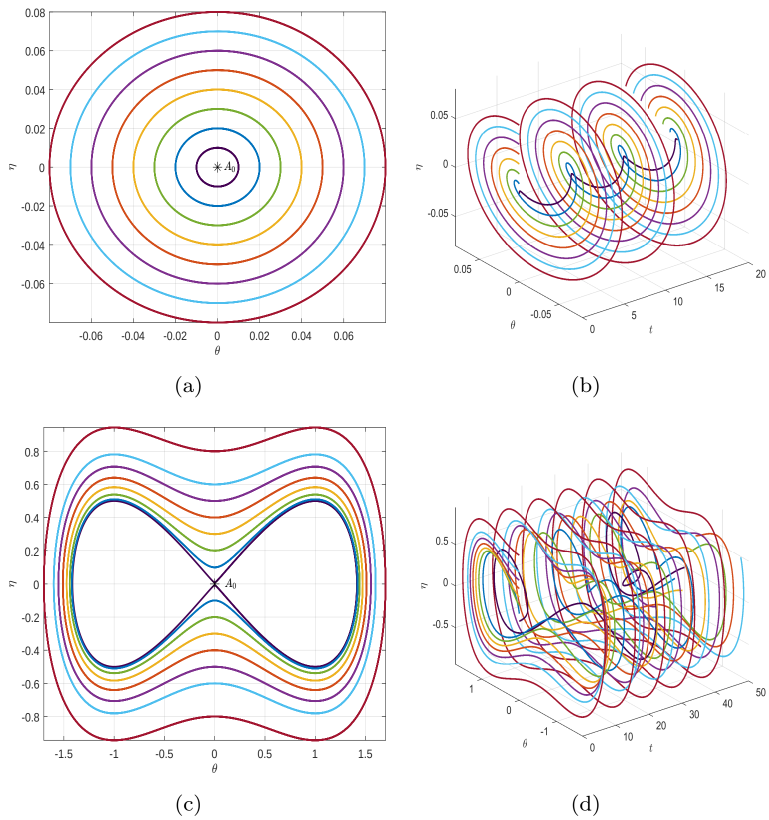

Figure 8. Figure (a)-(b) depict the phase diagrams and three-dimensional spatial diagrams corresponding to different initial conditions near $A_0(0,0)$, with the parameters $\lambda = 2$, $\mu = 1$ and $\omega = 1$. Figure (c)-(d) depict the phase diagrams and three-dimensional spatial diagrams corresponding to different initial conditions near $A_0(0,0)$, with the parameters $\lambda = 1$, $\mu = 1$ and $\omega = 2$.

shown in the two-dimensional phase diagram and three-dimensional spatial trajectory diagram corresponding to Figures 9(a) and 9(b). When the parameters are set to $\lambda = 2$, $\mu = -1$ and $\omega = 1$, the eigenvalues of the system are $\pm\sqrt{2}$, indicating that the system is unstable, and the corresponding equilibrium point A_1 is a saddle point. As the system evolves over a long period, it rapidly diverges outward. The specific two-dimensional and three-dimensional images can be referred to in Figure 9(c)-(d).

The study of whether a system exhibits chaos can be approached through phase diagrams on one hand, and through quantitative analysis on the other. The Lyapunov exponent serves as a crucial tool in this regard. It primarily determines the presence of chaos by measuring the system's divergence rate. When the Lyapunov exponent is greater than zero, the system's trajectories show a tendency to diverge rapidly, indicating instability. Conversely, when the Lyapunov exponent is less than zero, the system remains stable.

Figure 10(a) illustrates the scenario near equilibrium point $A_0 = (0,0)$ with initial conditions $(\theta, \eta) = (0, 0.1)$. Here, the Laypunov exponent is greater than 0, the equilibrium point acts as a saddle point, and the system exhibits unstable behavior. Figure 10(b) depicts the case near equilibrium point $A_1 = (1,0)$ with initial conditions $(\theta, \eta) = (1, 0.1)$, where the Lyapunov exponent is negative, confirming the system's stability. This observation aligns with the conclusion

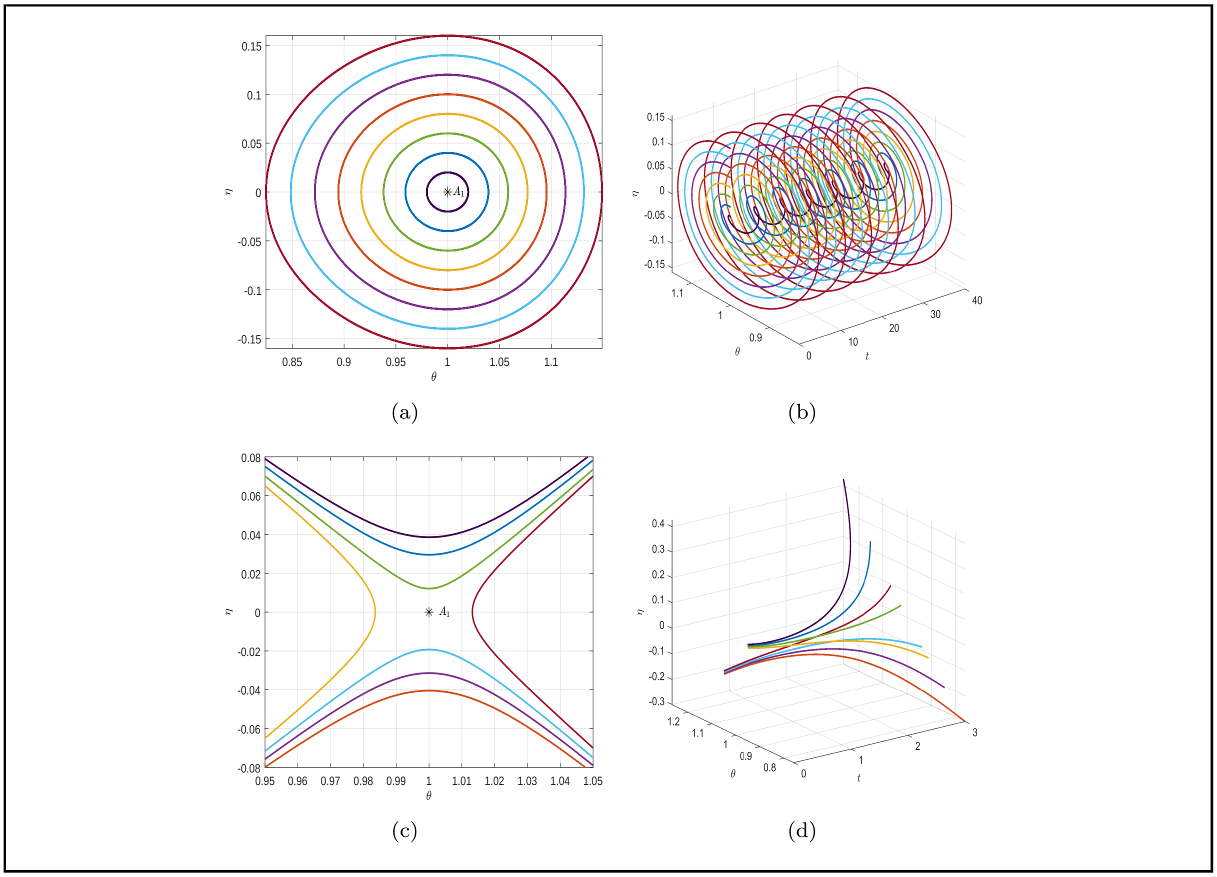

Figure 9. Figure (a)-(b) depict the phase diagrams and three-dimensional spatial diagrams corresponding to different initial conditions near $A_1(1,0)$, with the parameters $\lambda = 1$, $\mu = 1$ and $\omega = 2$. Figure (c)-(d) depict the phase diagrams and three-dimensional spatial diagrams corresponding to different initial conditions near $A_1(1,0)$, with the parameters $\lambda = 2$, $\mu = -1$ and $\omega = 1$.

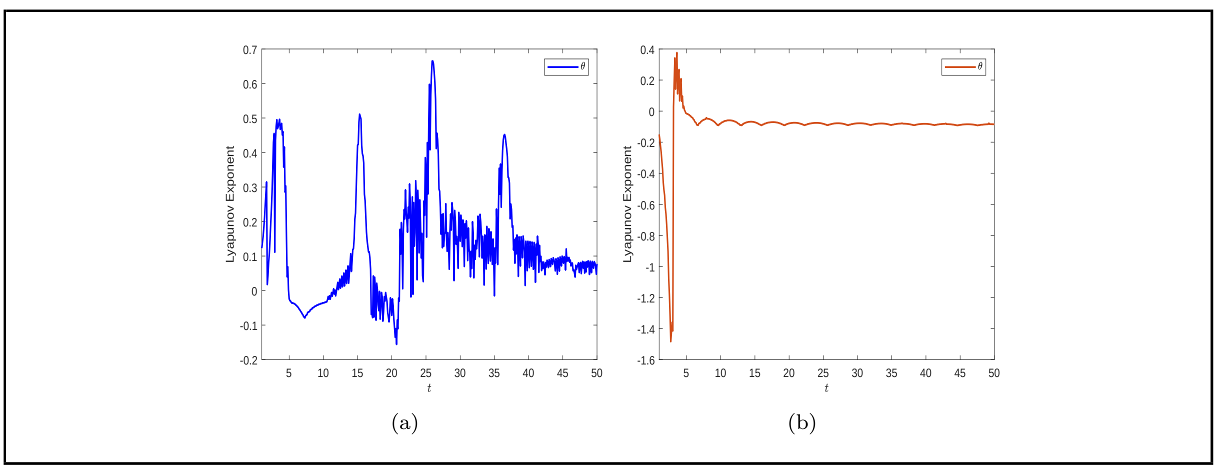

Figure 10. LE diagram. Figure(a) is the LE for trajectory corresponding to initial values near the equilibrium point $A_0(0,0)$. Figure(b) is the LE diagram for trajectory corresponding to initial values near the equilibrium point $A_1(1,0)$. Where $\lambda = 1$, $\mu = 1$ and $\omega = 2$.

that $A_1 = (1, 0)$ is a center point. Therefore, the Lyapunov exponent effectively assesses system stability and the presence of chaos.

4. Numerical results

While closed-form analytical solutions hold irreplaceable value for deeply understanding the fundamental principles of differential equations, they are often limited by idealized assumptions and frequently become impractical when dealing with complex nonlinear systems in real-world engineering. From a mathematical structure standpoint, differential equations of any order can be converted into systems of first-order equations via state-space transformation-this inherent property has transformed numerical methods from supplementary tools into essential technologies across modern engineering fields. [12, 15, 16]

To address the constraints of traditional analytical approaches, computational mathematics has been applied to find the numerical results. Following the transformation of the governing equations into first-order systems via state-space formulation, the trade-off between numerical integration accuracy and computational efficiency becomes critical. While the classical RK44 method is widely adopted for its implementation simplicity and computational economy, its fourth-order accuracy may prove insufficient for handling highly dynamic systems or long-term simulation scenarios. To address this limitation, the present study primarily employs the sixth-order Huta86 scheme (Huta86) [51], which possesses sixth-order accuracy. The initial conditions are constrained by the analytical result, specifically, the initial values used in the numerical computations of this paper are all determined by equation $\theta_{1.2}$ and the step size is $h1 = 0.1$, $h2 = 0.5$. By incorporating additional function evaluations, this algorithm significantly improves truncation error control and numerical stability, thereby enabling the capture of subtle system dynamics with higher confidence. Although Huta86 incurs greater computational cost than RK44, its superior precision provides reliable assurance for achieving the research objectives, making the additional computational investment both necessary and justified. The specific formulas of this method are as follows:

$$\begin{cases} G_1 = \theta(x_n, y_n), \\ G_2 = \theta(x_n + \frac{1}{9}h, y_n + \frac{1}{9}hG_1), \\ G_3 = \theta(x_n + \frac{1}{6}h, y_n + \frac{1}{24}h(G_1 + 3G_2)), \\ G_4 = \theta(x_n + \frac{1}{3}h, y_n + \frac{1}{6}h(G_1 - 3G_2 + 4K_3)), \\ G_5 = \theta(x_n + \frac{1}{2}h, y_n + \frac{1}{8}h(-5G_1 + 27G_2 - 24G_3 + 6G_4)), \\ G_6 = \theta(x_n + \frac{2}{3}h, y_n + \frac{1}{9}h(221G_1 - 981G_2 + 867G_3 - 102G_4 + G_5)), \\ G_7 = \theta(x_n + \frac{5}{6}h, y_n + \frac{1}{48}h(-183G_1 + 678G_2 - 472G_3 - 66G_4 + 80G_5 + 3G_6)), \\ G_8 = \theta(x_n + h, y_n + \frac{1}{82}h(716G_1 - 2079G_2 + 1002G_3 + 834G_4 - 454G_5 - 9G_6 + 72G_7)), \\ y_{n+1} = y_n + \frac{h}{840}(41G_1 + 216G_3 + 24G_4 + 272G_5 + 27G_6 + 216G_7 + 41G_8). \end{cases} \tag{4.1}$$

Figure 11(a) and (b) present the error distributions between numerical and analytical solutions for the absolute values of $\theta_{1.2}(x,t)$ obtained using the RK44 and Huta86 methods, respectively, while Figure 11(c) and (d) illustrate the corresponding error variations in polar coordinates. As the independent variable δ increases, the absolute error progressively accumulates due to error propagation effects. Nevertheless, Figures 19(c) and (d) clearly demonstrate that the maximum absolute error remains below 1×10^{-8} for the RK44 method and below 2×10^{-12} for the Huta86 method. These results further confirm that the Huta86 algorithm exhibits remarkable computational stability and achieves significantly enhanced numerical accuracy compared to the RK44 method.

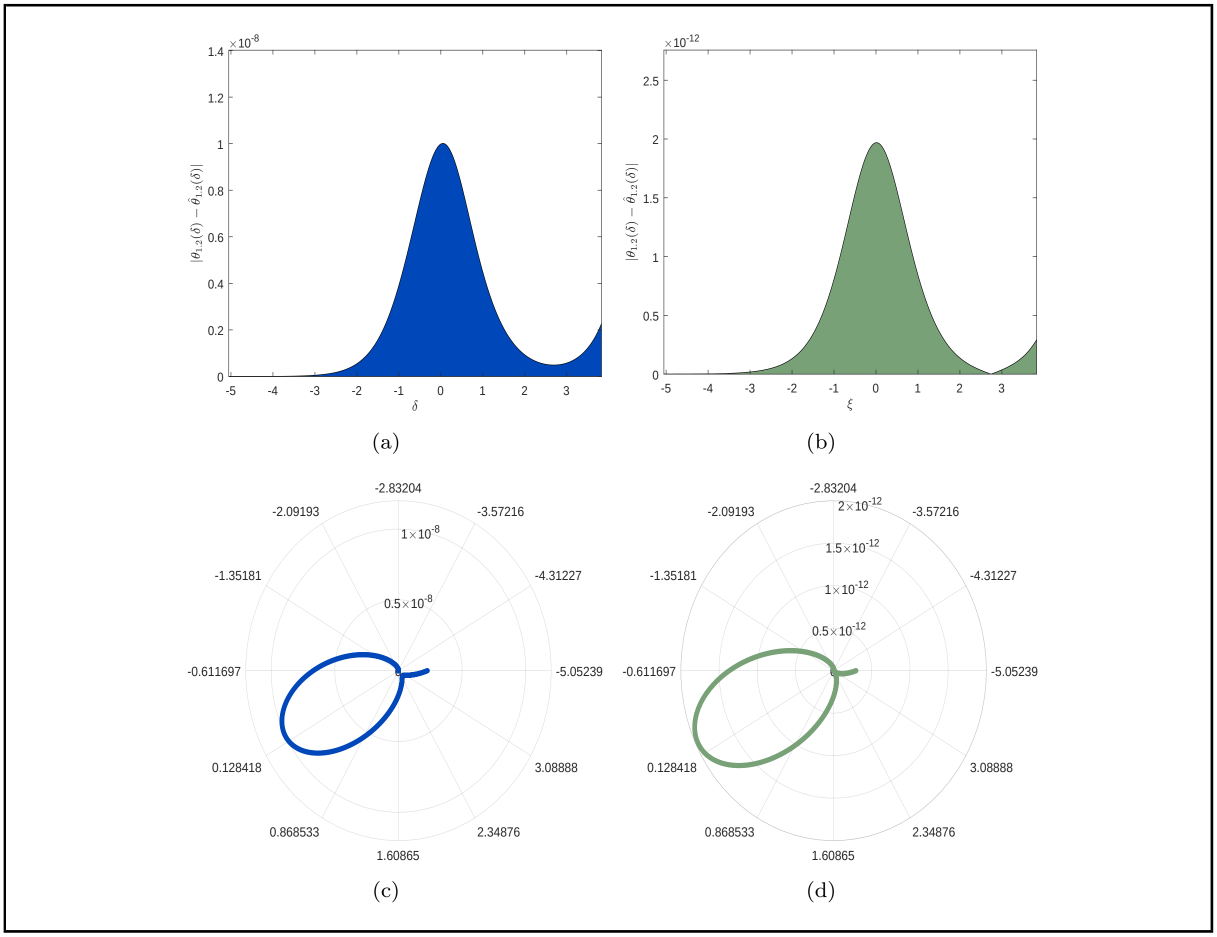

Figure 11. Figures (a) and (b) show the absolute error range between the numerical and analytical solutions of $\theta_{1.2}$ for the two methods, and Figures (c) and (d) present the corresponding polar coordinate diagrams.

Figure 12(a) and (b) present the numerical solutions of the physical quantity $\theta_{1.2}(x,t)$ obtained using the RK44 method and the Huta86 method, respectively. Through comparison with the corresponding analytical solutions, it can be observed that the numerical results exhibit remarkable consistency with theoretical expectations in terms of waveform, phase, and amplitude. This high degree of agreement not only validates the effectiveness of both numerical methods in solving this particular problem but also demonstrates their significant reliability in computational accuracy, thereby establishing a solid foundation for subsequent numerical analysis of related physical quantities. For details on the specific differences between the numerical and analytical solutions in local regions, refer to Tables 1 and 2.

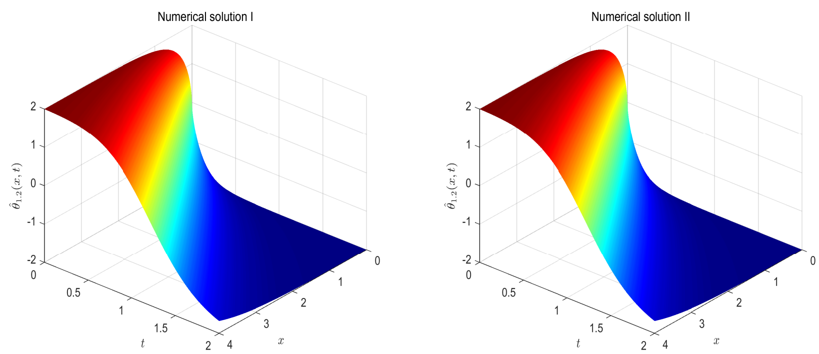

(a) (b)

Figure 12. Figures (a) and (b) show the numerical solutions of $\hat{\theta}_{1.2}$ obtained using the RK44 and Huta86 methods, respectively.

In Figure 13(a) and (b), we compare the absolute error performance of the classical RK44 and a high-precision numerical integration scheme Huta86 when solving a specific differential equation. The results demonstrate that the Huta86 method exhibits a significant advantage in controlling numerical errors. Its maximum absolute error is on the order of 2×10^{-10}, which is two orders of magnitude lower than the approximately 1×10^{-8} maximum error of the RK44 method. The Huta86 method not only maintains exceptionally high accuracy but also displays a complex, wave-like error distribution pattern. Although minor numerical oscillations are present, the method demonstrates good overall stability and high sensitivity to initial conditions. These findings indicate that the Huta86 method is the preferable choice for applications requiring high-precision numerical simulations, whereas RK44 is more suitable for scenarios where computational efficiency is prioritized over accuracy. This study provides valuable insights for further exploration of the applicability of different numerical integration strategies in solving complex dynamical problems.

The results of this study clearly demonstrate that the adopted eight-stage, sixth-order Huta algorithm possesses a solid theoretical foundation and exhibits outstanding accuracy in practical computations. This method not only effectively meets the stringent accuracy requirements of high-precision scientific simulations, but also firmly establishes itself as the preferred numerical solution strategy for addressing the complex scientific problems investigated in this work.

5. Conclusions

This study takes the SMCH equation with CFD as the core research object, achieving multiple innovations in the fields of shallow water wave dynamics modeling and fractional derivative application. Meanwhile, through comparison with the paper [42], its research value is further highlighted. From the perspective of core innovations, this paper applies the extended tanh-function method to the SMCH equation with CFD for the first time, breaking through the limitations

Table 1. The absolute errors between the numerical solution $\hat{\theta}_{1.2}(x,t)$ and the analytical solution $\theta_{1.2}(x,t)$ under the RK44 method in $(x,t) \in [0.5,4] \times [0,2]$.

	x=0.5	x=1.1	x=2.3	x=3.5	x=4
t=0	3.87717E-09	1.32329E-09	4.93539E-10	1.30274E-09	2.26906E-09
t=0.1	9.73905E-09	4.97280E-09	1.05495E-09	4.90331E-10	5.70329E-10
t=0.2	9.45827E-09	8.28678E-09	2.13525E-09	6.39361E-10	5.00667E-10
t=0.3	7.23680E-09	9.94520E-09	3.70848E-09	1.04698E-09	6.82675E-10
t=0.4	5.07974E-09	9.48494E-09	5.80814E-09	1.70083E-09	1.06251E-09
t=0.5	3.31559E-09	7.92242E-09	7.82765E-09	2.67414E-09	1.65515E-09
t=0.6	2.10606E-09	5.97999E-09	9.59300E-09	3.99425E-09	2.50854E-09
t=0.7	1.31574E-09	4.34137E-09	1.00221E-08	5.66206E-09	3.65624E-09
t=0.8	8.43955E-10	3.04134E-09	9.43143E-09	7.30921E-09	5.13046E-09
t=0.9	5.29013E-10	2.06876E-09	8.36624E-09	8.93377E-09	6.73005E-09
t=1.0	3.28594E-10	1.40398E-09	6.72888E-09	9.89705E-09	8.28614E-09
t=1.1	2.13347E-10	9.30077E-10	5.41002E-09	9.99086E-09	9.46743E-09
t=1.2	1.39112E-10	6.14415E-10	4.09239E-09	9.41772E-09	1.00321E-08
t=1.3	8.57470E-11	4.22901E-10	3.02388E-09	8.25846E-09	9.86039E-09
t=1.4	5.84406E-11	2.75549E-10	2.18991E-09	7.09806E-09	9.07592E-09
t=1.5	3.63225E-11	1.91158E-10	1.57746E-09	5.75794E-09	8.09584E-09
t=1.6	2.49727E-11	1.25358E-10	1.11221E-09	4.63173E-09	6.77798E-09
t=1.7	1.56410E-11	8.76510E-11	8.08051E-10	3.59864E-09	5.58550E-09
t=1.8	1.02038E-11	5.96971E-11	5.72340E-10	2.75455E-09	4.46312E-09
t=1.9	7.08744E-12	3.91385E-11	3.91531E-10	2.07156E-09	3.48269E-09
t=2.0	4.25904E-12	2.79139E-11	2.85352E-10	1.55268E-09	2.67616E-09

of existing studies—previous solutions for the SMCH equation mostly adopted methods such as the modified auxiliary equation method and the first integral method. The introduction of this method not only efficiently derives various analytical solutions, including single-peak solitons, composite double-peak solitons, single-peak with shoulder solitons, and periodic soliton trains, but also determines the formal order of the solutions through a rigorous homogeneous balance method to ensure the physical rationality of the solutions. This methodological innovation provides a new paradigm for solving similar fractional shallow water wave equations. In terms of exploring dynamic mechanisms, the paper goes beyond mere solution construction: It analyzes the center-saddle bifurcation characteristics of the system's equilibrium points through phase diagrams, and quantifies the system's chaotic behavior using Lyapunov exponents (e.g., a positive exponent at the equilibrium point $A_0 = (0,0)$ corresponds to an unstable saddle point, while a negative exponent at $A_1 = (1,0)$ corresponds to a stable center point). It is the first to reveal the evolution law of the SMCH equation with CFD from periodic motion to chaotic state, filling the gap in the research on the dynamic behavior of this equation in the [42]. Additionally, the paper innovatively uses two numerical methods, RK44 and the sixth-order accurate Huta86 scheme, to verify the analytical solutions through comparative analysis. Error analysis shows that the

Table 2. The absolute errors between the numerical solution $\hat{\theta}_{1.2}(x,t)$ and the analytical solution $\theta_{1.2}(x,t)$ under the Huta86 method in $(x,t) \in [0.5, 4] \times [0, 2]$.

	x=0.5	x=1.1	x=2.3	x=3.5	x=4
t=0	3.84315E-12	1.92066E-11	1.95177E-13	1.30096E-12	1.01521E-11
t=0.1	1.80672E-10	1.25433E-12	1.20286E-11	5.14921E-13	3.79208E-12
t=0.2	8.36613E-11	8.41037E-11	5.70877E-13	8.57692E-12	4.40536E-12
t=0.3	1.58912E-10	2.99812E-11	7.06324E-13	1.06466E-11	1.02194E-11
t=0.4	2.60254E-11	9.97496E-11	9.03446E-11	2.18030E-11	1.19225E-11
t=0.5	6.06204E-12	8.77716E-11	5.43765E-12	1.35232E-11	1.45428E-11
t=0.6	6.69731E-12	1.30128E-10	1.73239E-10	1.02929E-11	1.05072E-11
t=0.7	3.23985E-12	5.18010E-11	1.29946E-11	8.80462E-11	5.99298E-13
t=0.8	2.39868E-11	3.80362E-13	1.14799E-10	2.11651E-11	6.09088E-11
t=0.9	1.44509E-11	1.12292E-11	3.76765E-12	1.24848E-10	7.03233E-11
t=1.0	3.49187E-12	2.85796E-11	1.61452E-10	1.18218E-10	8.35291E-11
t=1.1	6.41287E-12	1.52982E-11	1.02518E-12	2.17913E-12	7.46311E-11
t=1.2	6.44684E-12	6.41376E-12	4.23528E-12	6.11777E-11	5.98544E-11
t=1.3	1.46994E-13	1.80613E-11	1.82721E-12	2.07500E-10	1.05496E-12
t=1.4	2.91234E-12	5.14611E-12	1.36957E-12	1.04813E-10	8.78942E-11
t=1.5	1.54543E-13	9.89431E-12	1.18281E-11	1.36148E-10	1.60660E-12
t=1.6	1.35314E-12	3.41083E-12	6.39044E-13	4.27767E-11	8.11007E-11
t=1.7	2.02283E-13	5.34062E-12	2.21658E-11	1.79585E-11	3.32725E-11
t=1.8	1.22347E-13	3.99059E-12	1.77713E-11	9.19398E-12	1.42821E-11
t=1.9	5.26468E-13	1.36446E-12	3.47944E-13	1.67653E-11	7.17693E-12
t=2.0	1.68754E-14	2.27396E-12	9.27192E-12	3.01437E-11	2.44071E-12

maximum absolute error of Huta86 is less than 2×10^{-12}, which is two orders of magnitude more accurate than RK44, providing rigorous numerical support for the engineering application of the analytical solutions.

Compared with [42], although both studies take the SMCH equation as the carrier and compare the simulation differences of different fractional derivative models through visualization, the innovation and research depth of this paper are significantly prominent: First, in terms of the research dimension of derivative models, the latter only focuses on the binary comparison between CFD and MFD, while this paper further introduces the MRLD to construct a "CFD-MFD-MRLD" ternary comparison system. This more comprehensively clarifies the influence of different derivative models on the simulation of shallow water wave velocity fields (e.g., CFD is superior to MFD and MRLD in local detail simulation, such as the amplitude ratio of the shoulder to the main peak in the single-peak with shoulder structure, and computational stability). It also clarifies for the first time that the high resolution of the CFD for the spatial variation of the velocity field stems from its local differentiability, while the truncation effect of MFD and the non-local property of MRLD easily lead to energy dispersion. Second, in terms of research scope, [42] focuses on the analysis of parameter effects on wave forms and solution construction,

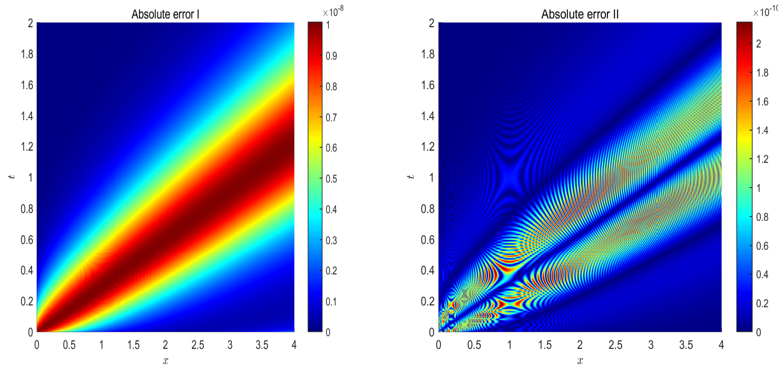

Figure 13. Figure (a) shows the absolute error performance of the classical RK44 method when solving the equation, and (b) shows that of the Huta86 method.

while this paper adds chaotic behavior analysis and multi-numerical method verification, forming a complete research chain of "analytical solution construction-dynamic mechanism-numerical verification-engineering application". In particular, it provides a quantitative tool for predicting the stability of shallow water wave systems through Lyapunov exponents, a research dimension not covered in [42]. Third, in the extension of engineering value, this paper associates the fractional order α with practical engineering scenarios (e.g., low α corresponds to weakly nonlinear waves in nearshore areas, and high α corresponds to strong solitary waves in ports). Combined with the dual regulatory effect of parameter ω on wave propagation direction and amplitude, it provides more accurate theoretical basis for breakwater design and wave load prediction. In contrast, the engineering relevance of [42] focuses more on parameter optimization and does not form a scenario-based application system. In summary, through methodological innovation, in-depth exploration of mechanisms, and multi-dimensional verification, this paper not only improves the fractional derivative solution system of the SMCH equation, but also achieves a breakthrough in connecting dynamic behavior with engineering applications. It complements [42] and is more pioneering in terms of innovation and research integrity.

Availability of data and materials. Not applicable.

Declaration of competing interest. The authors declare that they have no conflicts of interest.

Authors' contributions. All authors typed, read, and approved the final manuscript.

Acknowledgments. The work presented in this paper was supported by the National Natural Science Foundation of China (11326083).

References

[1] M. A. E. Abdelrahman and H. A. Alkhidhr, *Closed-form solutions to the conformable space-time fractional simplified MCH equation and time fractional Phi-4 equation,* Results Phys., 2020, 18, 103294.

[2] G. Akram, M. Sadaf, S. Arshed, et al., *Simulations of exact explicit solutions of simplified modified form of camassa-holm equation,* Opt. Quantum Electron., 2024, 56, 1037.

[3] S. Albeverio, Z. Brzeźniak and A. Daletskii, *Stochastic camassa-holm equation with convection type noise,* J. Differ. Equations, 2021, 276, 404–432.

[4] K. K. Ali and A.-H. Abdel-Aty, *An extensive analytical and numerical study of the generalized q-deformed Sinh-Gordon equation,* J. Ocean Eng. Sci., 2024, 9, 232–239.

[5] A. Bakhket, M. Fathi, M. Zakarya, et al., *Extensions of bicomplex hypergeometric functions and riemann-liouville fractional calculus in bicomplex numbers,* Fractal Fract., 2024, 8(9), 508.

[6] G. Barbero, L. R. Evangelista, R. S. Zola, et al., *A brief review of fractional calculus as a tool for applications in physics: Adsorption phenomena and electrical impedance in complex fluids,* Fractal Fract., 2024, 8(7), 369.

[7] H. M. Baskonus, A. A. Mahmud, K. A. Muhamad, et al., *A study on Caudrey-Dodd-Gibbon-Sawada-Kotera partial differential equation*, Math. Methods Appl. Sci., 2022, 45(14), 8737–8753.

[8] T. R. Biswas, S. Dey and D. Sen, *Modeling positive surge propagation in open channels using the Serre-Green-Naghdi equations,* Appl. Math. Modell., 2021, 97, 803–820.

[9] M. S. Bruzon, G. Gaetana and M. L. Gandarias, *Generalized camassa-holm equations: Symmetry, conservation laws and regular pulse and front solutions,* Mathematics, 2021, 9(9), 1009.

[10] H. Cakicioglu, M. Cinar, A. Secer, et al., *Optical solitons for kundu-mukherjee-naskar equation via enhanced modified extended tanh method,* Opt. Quantum Electron., 2023, 55, 400.

[11] R. Camassa and D. D. Holm, *An integrable shallow water equation with peaked solitons,* Phys. Rev. Lett., 1993, 71(11), 1661–1664.

[12] D. D. Cao and C. P. Li, *Quenching phenomenon in the caputo-hadamard time-fractional kawarada problem: Analysis and computation,* Math. Comput. Simul., 2025, 233, 21–38.

[13] C. H. Chang, C. H. Yu and T. W. H. Sheu, *Long-time asymptotic solution structure of camassa-holm equation subject to an initial condition with non-zero reflection coefficient of the scattering data,* J. Math. Phys., 2016, 57.

[14] W. S. Chang, M. M. Bazuhair, F. Ismail, et al., *Well-balanced energy-stable residual distribution methods for the shallow water equations with varying bottom topography,* Comput. Math. Appl., 2023, 148, 188–199.

[15] J. Chen, W. G. Sun and S. Zheng, *New predefined-time stability theorem and synchronization of fractional-order memristive delayed BAM neural networks,* Commun. Nonlinear Sci., 2025, 148, 108850.

[16] J. Chen, W. G. Sun and S. Zheng, *Encrypting images using multiple fractional-order drive-response systems with practical finite-time synchronization,* Math. Comput. Simul., 2026, 240, 423–437.

[17] Q. L. Chen, H. M. Baskonus, W. Gao, et al., *Soliton theory and modulation instability analysis: The Ivancevic option pricing model in economy,* Alexandria Eng. J., 2022, 61(10), 7843–7851.

[18] R. Chen, Z. C. Yang and S. M. Zhou, *Existence and uniqueness of the global conservative weak solutions for a cubic camassa-holm type equation,* J. Differ. Equations, 2024, 386, 480–518.

[19] D. Chou, S. M. Boulaaras, H. U. R. Rehman, et al., *Probing wave dynamics in the modified fractional nonlinear schrödinger equation: Implications for ocean engineering,* Opt. Quantum Electron., 2024, 56, 228.

[20] M. Cinar, I. Onder, A. Secer, et al., *Soliton solutions of* $(2+1)$*-dimensional heisenberg ferromagnetic spin equation by the extended rational* $\sin-\cos$ *and* $\sinh-\cosh$ *method,* Int. J. Appl. Comput. Math., 2021, 7(4), 1–17.

[21] M. Cinar, I. Onder, A. Secer, et al., *Solving the fractional Jaulent-Miodek system via a modified Laplace decomposition method,* Waves Random Complex Medium., 2022, 35(2), 4036–4049.

[22] P. A. Clarkson and T. J. Priestley, *Shallow water wave systems,* Stud. Appl. Math., 1998, 101(4), 389–432.

[23] S. B. Dai, X. Li, J. M. Hou, et al., *Numerical study of critical flow for seven types of weirs affected by dam-break like rapidly varied flow,* Phys. Fluids, 2025, 37(3), 036631.

[24] A. Degasperis and G. Gaeta, *Asymptotic integrability. In symmetry and perturbation theory,* World Scientific, 1999, 23–37.

[25] I. K. Delia, *Variational derivation of a geophysical camassa-holm type shallow water equation,* Nonlinear Anal., 2017, 156, 286–294.

[26] W. Y. Duan, K. Zheng, B. B. Zhao, et al., *On wave–current interaction by the green–naghdi equations in shallow water,* Nat. Hazard., 2016, 83(1), 547–570.

[27] H. Emamirad and A. Rougirel, *Delsarte equation for caputo operator of fractional calculus,* Fract. Calc. Appl. Anal., 2022, 25, 584–607.

[28] G. Failla and M. Zingales, *Advanced materials modelling via fractional calculus: Challenges and perspectives,* Philos. T. R. Soc. A, 2020, 378(2172).

[29] B. Fornberg and G. Whitham, *A numerical and theoretical study of certain nonlinear wave phenomena,* Philos. T. R. Soc. A., 1978, 289(1361), 373–404.

[30] A. E. Green and P. M. Naghdi, *A derivation of equations for wave propagation in water of variable depth,* J. Fluid Mech., 1976, 78(2), 237–246.

[31] A. E. Green and P. M. Naghdi, *Water waves in a nonhomogeneous incompressible fluid,* J. Appl. Mech., 1977, 44(4), 523–528.

[32] M. N. Islam, M. Asaduzzaman and M. S. Ali, *Exact wave solutions to the simplified modified camassa-holm equation in mathematical physics,* AIMS Math., 2020, 5(1), 26–41.

[33] S. Javeed, M. A. Abbasi, T. Imran, et al., *New soliton solutions of simplified modified camassa holm equation, klein-gordon-zakharov equation using first integral method and exponential function method,* Results Phys., 2022, 38, 105506.

[34] M. Khalighi, L. Eftekhari, S. Hosseinpour, et al., *Three-species lotka-volterra model with respect to caputo and caputo-fabrizio fractional operators,* Symmetry, 2021, 13(3), 368.

[35] R. Khalil, M. Al Horani, A. Yousef, et al., *A new definition of fractional derivative,* J. Comput. Appl. Math., 2014, 264, 65–70.

[36] D. A. Koç, S. Kilbitmez and H. Bulut, *The new complex travelling wave solutions of the simplified modified camassa holm equation,* Opt. Quantum Electron., 2024, 56, 215.

[37] J. Koellermeier and E. Pimentel, *Steady states and well-balanced schemes for shallow water moment equations with topography,* Appl. Math. Comput., 2022, 427, 127166.

[38] D. Lannes, *Modeling shallow water waves,* Nonlinearity., 2020, 33(5).

[39] J. Li, Y. Liu and Q. L. Wu, *Spectral stability of smooth solitary waves for the degasperis-procesi equation,* J. Math. Pures Appl., 2020, 142, 298–314.

[40] M. Lin, *Well-posedness and infinite propagation speed for the fifth-order camassa-holm equation with weakly dissipative term,* J. Appl. Math. Phys., 2023, 11(3).

[41] L. Mescia, P. Bia, D. Caratelli, et al., *Fractional-calculus-based electromagnetic tool to study pulse propagation in arbitrary dispersive dielectrics,* Phys. Status Solidi A, 2018, 216(3), 1800557.

[42] I. Onder, M. Cinar, A. Secer and M. Bayram, *Analytical solutions of simplified modified camassa-holm equation with conformable and M-truncated derivatives: A comparative study,* J. Ocean Eng. Sci., 2024, 9, 240–250.

[43] I. Onder, M. Cinar, A. Secer, et al., *Comparative analysis for the nonlinear mathematical equation with new wave structures,* Eur. Phys. J. Plus, 2022, 137, 1120.

[44] L. A. Ostrovsky, *Nonlinear internal waves in a rotating ocean,* Oceanologia, 1978, 18(2), 181–191.

[45] M. Ozisik, M. Cinar, A. Secer, et al., *Optical solitons with Kudryashov's sextic power-law nonlinearity,* Optik., 2022, 261, 169202.

[46] M. Ozisik, A. Secer and M. Bayram, *On the analytical optical soliton solutions of perturbed radhakrishnan-kundu-lakshmanan model with Kerr law nonlinearity,* Opt. Quantum Electron., 2022, 54, 371.

[47] Y. Pandir and A. Yildirim, *Analytical approach for the fractional differential equations by using the extended tanh method,* Waves Random Complex Medium., 2018, 28(3), 399–410.

[48] K. R. Raslan, K. K. Ali and M. A. Shallal, *The modified extended tanh method with the riccati equation for solving the space-time fractional EW and MEW equations,* Chaos Soliton Fract., 2017, 103, 404–409.

[49] M. Sahoo and S. Chakraverty, *Analyzing wave structure and bifurcation in geophysical boussinesq-type equations,* Phys. Fluids, 2024, 36(7), 077164.

[50] M. Sahoo and S. Chakraverty, *Time-fractional shallow water wave equation with fuzzy uncertainty,* Phys. Fluids, 2025, 37(5), 057112.

[51] D. Sarafyan, *Improved sixth-order runge-kutta formulas and approximate continuous solution of ordinary differential equations,* J. Math. Anal. Appl., 1972, 40(2), 436–445.

[52] J.-C. Saut, S. Sun, Y. Wang, Y. Zhang, et al., *Wave breaking for the generalized fornberg–whitham equation,* SIAM J. Math. Anal., 2024, 56(4).

[53] M. A. Shallal, H. N. Jabbar and K. K. Ali, *Analytic solution for the space-time fractional klein-gordon and coupled conformable boussinesq equations,* Results Phys., 2018, 8, 372–378.

[54] O. El-Shamy, R. El-barkoki, H. M. Ahmed, et al., *Extraction of solitons in multimode fiber for CHNLSEs using improved modified extended tanh function method,* Alexandria Eng. J., 2024, 106, 403–410.

[55] S. Sol, *Analysis of the generalized ostrovsky equation in the propagation of surface and internal waves in rotating fluids,* Math. Methods Appl. Sci., 2025. DOI: 10.1002/mma.11036.

[56] H. G. Sun, Y. Zhang, D. Baleanu, et al., *A new collection of real world applications of fractional calculus in science and engineering,* Commun. Nonlinear Sci., 2018, 64, 213–231.

[57] T. Tanriverdi, H. M. Baskonus, A. A. Mahmud and K. A. Muhamad, *Explicit solution of fractional order atmosphere-soil-land plant carbon cycle system,* Ecol. Complex., 2021, 48, 100966.

[58] I. Y. Miranda-Valdez, J. G. Puente-Córdova, F. Y. Rentería-Baltiérrez, et al., *Viscoelastic phenomena in methylcellulose aqueous systems: Application of fractional calculus,* Food Hydrocolloids, 2024, 147(Part A), 109334.

[59] H. Q. Wang, *Some properties of the solutions of the N-component camassa-holm system with peakons,* Monatsh. Math., 2023, 201, 499–545.

[60] K. L. Wang and C. F. Wei, *Fractal soliton solutions for the fractal-fractional shallow water wave equation arising in ocean engineering,* Alexandria Eng. J., 2023, 65, 859–865.

[61] X. Wang, J. Wu, Y. Wang, et al., *Extended tanh-function method and its applications in nonlocal complex mKdV equations,* Mathematics, 2022, 10(18), 3250.

[62] A.-M. Wazwaz, *Solitary wave solutions for modified forms of degasperis-procesi and camassa-holm equations,* Phys. Lett. A, 2006, 352(6), 500–504.

[63] J. R. Wu, Z. Ji, K. C. Zhang, et al., *A new estimation of box dimension of riemann-liouville fractional calculus of continuous functions,* Fractals, 2024, 32(2), 2440005.

[64] H. Yang, *Non-uniform continuity of the solution map to the rotation-two-component camassa-holm system,* J. Differ. Equations, 2020, 268(8), 4423–4463.

[65] H. Y. Zhang and Y. F. Zhang, *Inverse scattering transform for integrable nonisospectral hierarchy associate with camassa-holm equation,* J. Geom. Phys., 2024, 204, 105276.

[66] Z. X. Zhang and Q. P. Liu, *On a two-component camassa-holm equation,* Appl. Math. Lett., 2025, 165, 109502.

Received March 2026; Accepted June 2026; Available online July 2026.